Materials Advances

ROYAL SOCIETY OF CHEMISTRY

PAPER

View Article Online
View Journal

Check for updates

Cite this: DOI: 10.1039/d5ma01042j

Effect of carbide on wear mechanisms at 300 °C of composite coatings sprayed by HVOF

Alejandra Islas Encalada, *[a] Pantcho Stoyanov,[b] Mary Makowiec,[c] Christian Moreau[d] and Richard R. Chromik *[a]

Evaluation of the wear behavior of composite coatings based on Stellite 6 with additions of WC-Ni and Cr_3C_2, produced *via* high-velocity oxygen fuel (HVOF) spraying at an elevated temperature. Evaluation of the effects of these carbides on the wear mechanism and to determine their impact on the formation of protective tribolayers. Stellite 6, a cobalt-based alloy, is widely known for its resistance to wear and corrosion, and the incorporation of carbides such as WC-Ni and Cr_3C_2 further enhances these properties. Two types of composite coatings were developed: SW (Stellite 6 with WC-Ni) and SWC (Stellite 6 with WC-Ni and Cr_3C_2). Microstructural analysis revealed that the carbides were uniformly distributed in the Stellite 6 matrix, with higher hardness and improved wear performance compared to similar coatings without carbides. Wear tests were conducted at room temperature and 300 °C. The results indicate that both coatings exhibit low wear rates caused by different wear mechanisms when tested at elevated temperatures.

Received 10th September 2025,
Accepted 30th November 2025

DOI: 10.1039/d5ma01042j

rsc.li/materials-advances

Introduction

The demand for coatings that provide excellent wear resistance at both room and elevated temperatures has driven advancements in thermal spray technologies, particularly high-velocity oxygen fuel (HVOF) spraying.[1] Wear-resistant coatings protect surfaces in industrial machinery and components that operate under harsh conditions, such as high temperatures and mechanical stresses.[2] Studies have shown that the formation of protective tribolayers during sliding wear, particularly at elevated temperatures, can significantly influence the wear performance of coatings.[3–7]

Stellite 6 is a cobalt–chromium alloy known for its superior wear and corrosion resistance due to the formation of hard carbides such as M_7C_3 during solidification.[8,9] However, these carbides do not form during the rapid solidification associated with HVOF spraying.[10,11] The addition of carbides to the Stellite 6 matrix has the potential to further improve these properties by increasing the overall hardness of the coating and promoting the formation of protective oxides during wear.[12,13]

Carbides like WC and Cr_3C_2, when embedded in a metal matrix, provide excellent wear resistance due to their high hardness and ability to resist deformation under mechanical stress.[14–16] WC-based coatings have been extensively studied and are commonly used in wear-resistant applications, offering excellent performance at room temperature and moderate temperatures.[12,17,18] However, WC can suffer from decarburization at higher temperatures, negatively impacting its wear resistance. On the other hand, Cr_3C_2 is more stable at elevated temperatures and has been shown to improve wear resistance.[19,20] In commercial applications, WC and Cr_3C_2 are typically used in coatings with metallic binders such as Ni, Co, or NiCr.[21–26]

HVOF spraying is a thermal spray process known for producing dense, high-quality coatings with low porosity and minimal oxidation.[27–29] The process involves propelling a mixture of powder and fuel gas at supersonic speeds onto a substrate, resulting in strong adhesion and minimal thermal degradation of the feedstock materials.[1,30] Therefore, HVOF is an ideal method for depositing coatings containing carbides, as it preserves the integrity of the carbide particles, preventing excessive decomposition and ensuring their uniform distribution within the matrix.[28,31] Previous studies on coatings with the addition of different carbides (*i.e.*, WC, TiC, Cr_3C_2) have demonstrated superior wear resistance and mechanical properties.[14,15,32] This improvement is associated with the interaction between the load-bearing capacity of the hard phase and the modification of the third bodies formed during wear.[33] Despite the extensive research on WC and Cr_3C_2-based

---

[a] *Department of Mining and Materials Engineering, McGill University, M.H. Wong Building, 3610 University Street, Montreal, Quebec, H3A 0C5, Canada. E-mail: richard.chromik@mcgill.ca*

[b] *Mechanical, Industrial and Aerospace Engineering, Concordia University, EV Building, 1515 St. Catherine W., Montreal, Quebec, H3G 2W1, Canada*

[c] *Pratt & Whitney, 400 Main Street, East Hartford, CT 06118, USA*

[d] *Chemical and Materials Engineering, Concordia University, EV Building, 1515 St. Catherine W., Montreal, Quebec, H3G 2W1, Canada*

coatings, the impact of using both carbides within a Stellite 6 matrix hasn't been thoroughly investigated, especially regarding how third bodies form in HVOF-sprayed coatings.[21,34]

In a prior study, the performance of a Stellite 6 coating was compared with that of a coating including chromium carbide at both room temperature and 300 °C, and the formation of a protective oxide film at higher temperatures was observed with the inclusion of carbides.[35] This study investigates the wear behavior of composite coatings based on Stellite 6 with additions of WC-Ni and Cr_3C_2–WC-Ni, produced by HVOF, at an elevated temperature of 300 °C. Specifically, the study seeks to evaluate the effect of these carbides on the formation of protective tribolayers and their influence on the wear resistance of the coatings.

Methodology

Composite coatings were produced from a mix of ceramic and metallic powders, specifically gas-atomized Stellite 6 (Eutectic Powders, Canada), chromium carbide (Eutectic Powders, Canada) and agglomerated and sintered WC-Ni powder (AMPERIT® 547, H.C. Starck, Germany). The particle size distribution of each powder was measured and characterized before proceeding with the coating deposition process using a laser diffraction analyzer (Microtrac, Germany). The morphology of each powder was examined using a scanning electron microscope (SEM, SU3500, Hitachi, Japan). X-ray diffraction (Co source, λ = 1.78897 Å, D8, Discovery Diffractometer, Bruker, USA) was used to further analyze the Stellite 6 powder and determine its phases, while its cross-section was used to obtain its microstructure using the ECCI mode (SU8300, Hitachi, Japan).

The coatings were produced using the high-velocity oxygen-fuel (HVOF) spraying technique, a method renowned for creating dense, high-quality coatings. The spraying parameters are presented in Table 1. Two composite coatings were designed using a metallic matrix in addition to one or two types of carbides. The first coating contained a blend of Stellite 6 and WC-Ni powders, while the second was a composite of Stellite 6, WC-Ni, and Cr_3C_2 powders. The corresponding volume percentage in the powder mix is presented in Table 2. Different compositions aimed at 60 vol% of the main carbide in the as-spray coating.[35] The deposition efficiency for each coating was measured as the weight gain divided by the mass of powder sprayed.

The coatings underwent metallographic preparation post-deposition to achieve a smooth, polished surface. This process involved multiple steps of polishing, starting with 9 μm, 3 μm and 1 μm diamond suspension, and finishing with 0.05 μm colloidal silica to ensure a high-quality surface finish. The phase composition of the coatings was evaluated using scanning electron microscopy (SEM) coupled with energy-dispersive X-ray spectroscopy (EDS), enabling the quantification of phase percentages across the cross-section of the coatings. Additionally, Vickers hardness tests were performed on the top surface of each coating at both ambient room temperature and elevated temperatures of 300 °C, utilizing a Microcombi tester (Anton Paar, Austria).

Table 1 Spray parameters for SW and SWC coatings

Parameter	Value
Feed rate (g min^{-1})	23
Number of passes	35
Oxygen flow rate (LPM)	304
Propylene flow rate (LPM)	79
Air flow rate (LPM)	422
Transverse speed (mm s^{-1})	1000

Table 2 Volume percentage in the powder mixture for spraying

	Percentage in powder mixture (vol%)		
Coating	Stellite 6	WC-Ni	Cr_3C_2
SW	44	56	—
SWC	20	10	70

Wear resistance of the coatings was conducted in a ball-on-flat configuration featuring a reciprocating motion. These tests were systematically performed at both room temperature and at elevated temperatures of 300 °C on polished samples using a heating stage. The temperature was measured on the surface of the sample before and after the test using a thermocouple. The parameters for the wear tests comprised a 10 mm track length, a normal load of 5 N, and a test frequency of 1 Hz, resulting in a maximum sliding speed of 3.14 cm s^{-1}. An Al_2O_3 ball was used as a counterbody of 6.35 mm diameter. This configuration was explicitly selected to mimic conditions similar to those in previous studies with composites.[35] The volume loss of the wear tracks was measured using light profilometry (NewView, Zygo Corporation, USA). An average cross-sectional worn area was calculated from the areas under the curves for a minimum of 30 depth profiles, which were extracted perpendicular to the sliding direction (see Fig. S1 in SI for more information). The average of the 30 measurements was then multiplied by the track length to obtain a measure of wear volume for the test. The wear rate was calculated by normalizing the wear volume to the normal load and total sliding distance. Volume loss of counterbodies were measured with the same profilometer by comparison and subtraction of an ideal sphere with 6.35 mm diameter (see Fig. S2 in SI for more information).

SEM-EDS and Raman spectroscopy were employed to analyze the effects of wear on the coating materials and obtain insights into the phase changes occurring within the worn regions. Raman measurements were carried out using an InVia spectrometer (Renishaw, UK) with an Ar+ ion laser source operating at a wavelength of 514.5 nm. A minimum of four measurements were taken at different points within the worn areas to ensure the reliability and reproducibility of the spectral data collected.

Results

The particle size distribution and morphology of the powders used in the coatings are shown in Fig. 1. The three powders

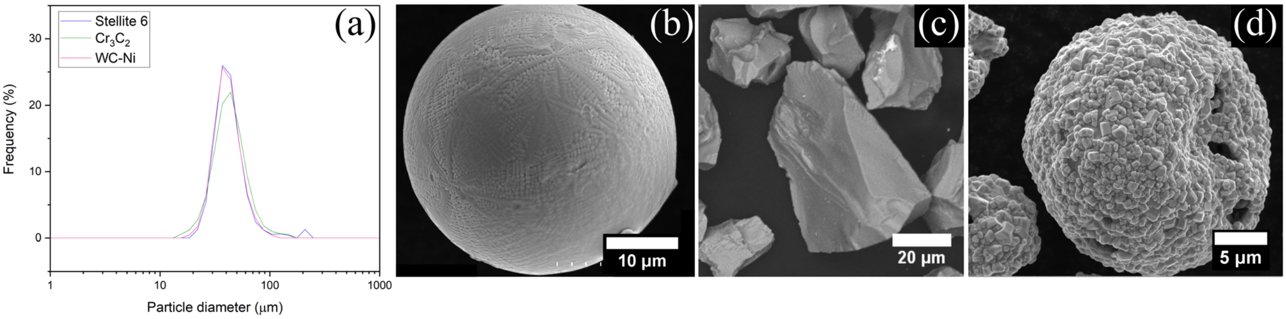

Fig. 1 (a) Particle size distribution of the powder feedstock and micrographs of the (b) Stellite 6, (c) chromium carbide and (d) tungsten carbide with nickel binder.

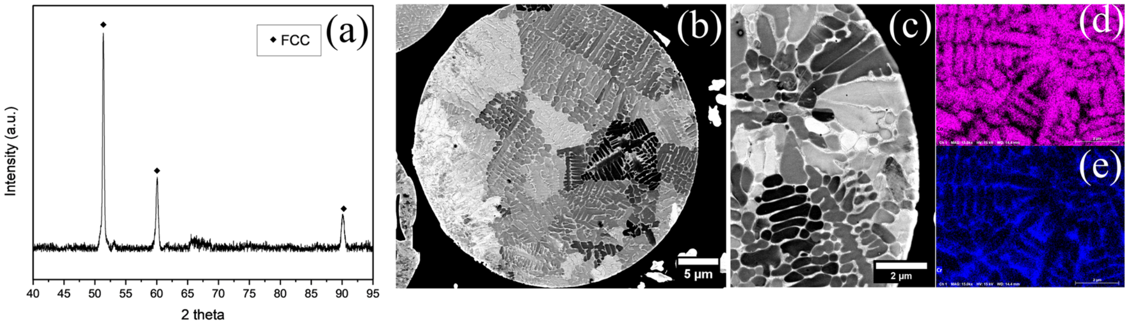

Fig. 2 Stellite 6 powder characterization. (a) XRD spectra. (b) Low magnification, (c) higher magnification and elemental distribution of a particle's cross section. (d) refers to cobalt content and (e) chromium.

(metallic matrix, agglomerated-tungsten carbide, and chromium carbide) exhibit similar particle size distributions (Fig. 1a), with D50 values of 34 μm, 37 μm, and 37 μm, respectively. According to XRD analysis (Fig. 2a), the Stellite 6 powder exhibits an FCC structure, and SEM images (Fig. 2b–e) show a dendritic structure with an inner Co core and an outer Cr layer.

These powders were combined to create two distinct composite coatings, labelled SW and SWC. The first coating, SW, was designed with a mixture of 30 wt% metal and 70 wt% tungsten carbide (44 vol% metal and 56 vol% carbide). The second coating, SWC, was a blend of 20 wt% metal, 60 wt% WC-Ni, and 20 wt% Cr_3C_2 (20 vol% metal, 10 vol% WC-Ni, and 70 vol% Cr_3C_2).

A summary of the coatings' properties, including deposition efficiency (DE), volume fractions of matrix and carbide, and porosity, is provided in Table 3. The retention of chromium carbide in the SWC coating was lower than that of tungsten carbide, which resulted in a decreased DE for this coating. Lower DE shows the higher compatibility of WC-Ni with the deposition process, leading to a larger retention within the coating. Hardness measurements at both room temperature (RT) and elevated temperatures (300 °C) are also presented in Table 3. These values are higher than those of comparable coatings without the carbide addition.[35] The hardness of the SWC coating, with a higher total carbide content, is higher than that of the SW coating at both RT and elevated temperatures. Both coatings show a lower hardness when tested at elevated temperatures (300 °C) related to the thermal softening of the metallic matrix and binder.[35]

Fig. 3 and 4 present micrographs of the coatings' cross-sections, showing the deposited materials' morphology. The electron channeling contrast imaging (ECCI) of the metallic splat's microstructure, as presented in Fig. 3b, reveals an absence of dendritic features, a result of the thermal input during the spraying procedure, which contrasts with the powder feedstock (Fig. 3b). Furthermore, the coating cross sections exhibited a well-bonded structure and homogeneously

Table 3 Properties of as-sprayed coatings

		Percentage in coating (vol%)				Hardness ($HV_{0.3}$)	
Coating	DE (%)	Stellite 6	WC-Ni	Cr_3C_2	Porosity	RT	300 °C
SW	75	37 ± 4	61 ± 4	—	3 ± 0.3	800 ± 123	693 ± 96
SWC	40	24 ± 2	17 ± 1	58 ± 2	1 ± 0.7	918 ± 114	820 ± 64

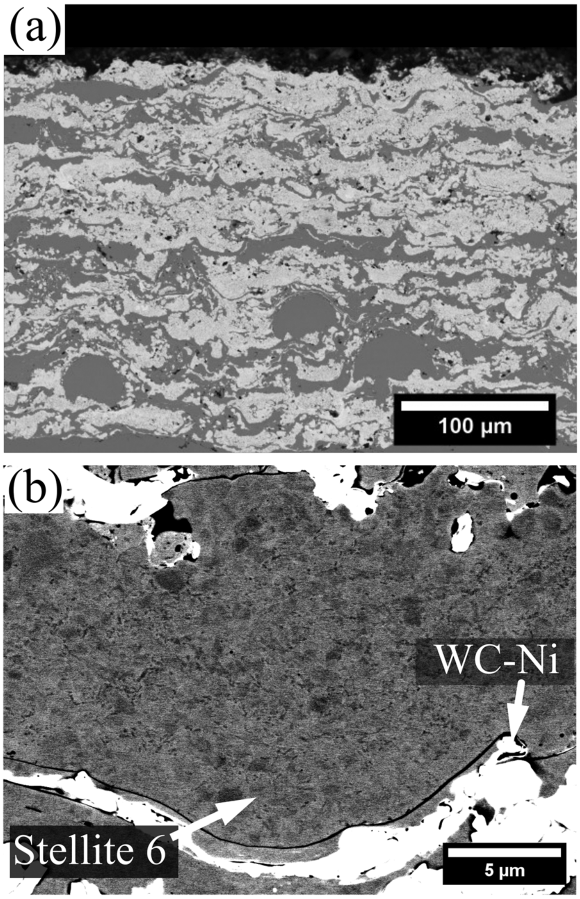

Fig. 3 (a) Cross-section morphology of the SW coating and (b) details of its constituents.

distributed metallic splats and deformed carbide particles. No evidence of phase segregation or agglomeration was observed, indicating that the carbides and the metallic matrix were evenly dispersed throughout the coating. In terms of brightness contrast in the micrographs, WC-Ni appeared as the brightest phase (light grey), followed by the metallic splats (medium grey), while Cr_3C_2 showed the darkest appearance (dark grey). This contrast highlights the compositional differences between the phases.

The average coefficient of friction (CoF) as a function of the number of cycles and the wear rate at room temperature are presented in Fig. 5, and the results at 300 °C are shown in Fig. 6 (see Fig. S3 to S8 for the curve of each repeat in the SI). At room temperature, both coatings exhibited higher CoF values during the run-in period, followed by a steady state throughout the wear tests, with only minor differences in wear rate. However, significant differences were observed at 300 °C. Compared to the results at room temperature, the fluctuation of CoF can be attributed to the formation and recirculation of debris at the interface, which is more significant for the SWC coating. A reduction in the coefficient of friction for the SWC coating is observed at approximately cycle 7500. Additionally, a reduction in wear rate values from 35 to 17 ($\times 10^{-6}$ mm^3 N^{-1} m^{-1}) was observed. Therefore, the presence of chromium carbide in SWC coating led to the formation of a protective tribolayer. The tribolayer, confirmed by EDS mapping and point analysis, consisted primarily of oxide phases that protected the surface from further damage during wear. The protective tribolayer's development was essential in transitioning the wear mechanism from severe to mild at elevated temperatures. In contrast, with a higher proportion of tungsten carbide, the SW coating

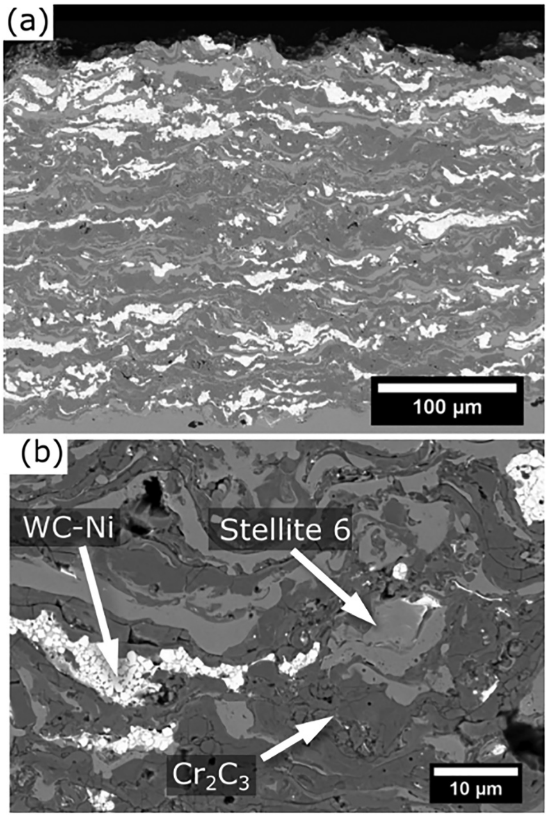

Fig. 4 (a) Cross-section morphology of SCW coating and (b) details of its constituents.

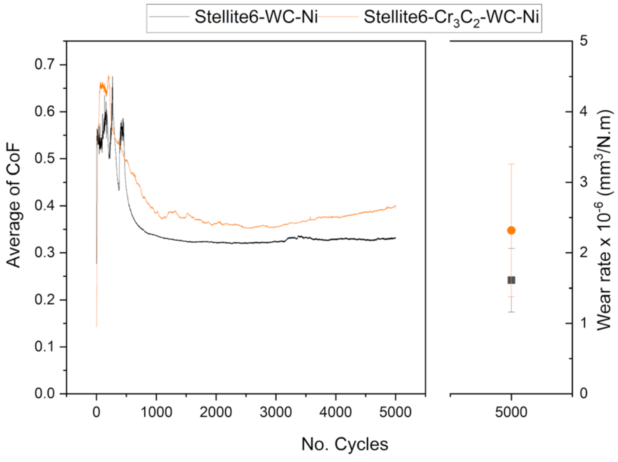

Fig. 5 Average of coefficient of friction *versus* number of cycles and wear rate at RT.

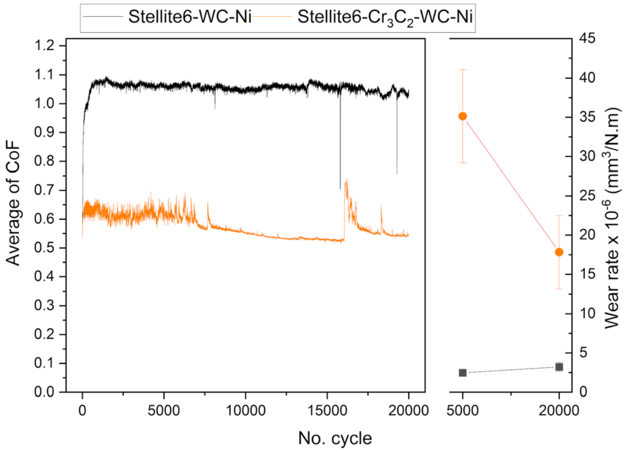

Fig. 6 Average of coefficient of friction *versus* number of cycles and wear rate at 300 °C.

demonstrated less tribolayer formation, leading to increased wear under the same conditions from 5000 to 20 000 cycles. The SW coating's wear rate was substantially lower than the SWC coating's, despite the latter's protective tribolayers. The SW coating wear rate is lower by an order of magnitude after 5000 cycles and 80% following 20 000 cycles.

The effect of the carbides in the coatings is essential in understanding their wear mechanisms. At room temperature, the carbides provided the load-bearing capacity within the SW and SWC coatings, presenting mainly abrasive marks on the metallic matrix (Stellite 6 splats), suggesting that the carbides protected the matrix from significant damage as observed in Fig. 7a and d, respectively. Fig. 7b and e highlight the formation of tribolayers mainly found at the centre of the wear track. For both coatings, the tribolayer is rich in Co, Cr and O (Fig. 7c and f). The oxide tribolayers in the SWC coating are larger (Fig. 7b and e), with signs of particle pull-out observed in the wear track (Fig. 7d), in comparison to the SW coating.

At elevated temperatures (300 °C), the SW coating presents mainly adhesive wear, with some traces of abrasive wear. Fig. 8b mostly shows metallic (Stellite 6) splats with abrasive marks and tongue-shape-like deformation. Therefore, the low volume loss of SW coatings can be related to the material's pull-out and minimal oxidative tribolayer formation, as observed in Fig. 8c (approx. 20 μm in length). For this tribolayer, Co, Cr, W and O were detected, and the presence of W is different from the results at room temperature. On the contrary, the tribolayer formation on the SWC coating was predominant. The higher wear rate at 5000 cycles is linked to the generation of wear debris that is eventually compacted into the tribolayer. A drop in CoF from 5000 to 20 000 cycles (Fig. 6) can be attributed to the protective nature of this tribolayer. Fig. 8f highlights a transition area of the tribolayer where un-sintered debris is observed, and smoother regions are observed at the centre. Fig. 8g and h demonstrate that the tribolayer expanded over the different phases present; for instance, tungsten from the carbide can be detected under the tribolayer. Therefore, chromium carbide contributed to wear resistance by promoting the formation of the oxide-based tribolayer at 300 °C after 7500 cycles.

After sliding at 300 °C for 20 000 cycles, different locations across the wear track were measured using Raman spectroscopy. Fig. 9a shows a mixture of binary and ternary oxides present on the SW coating. Peaks attributed to Co_3O_4 are clearly identified; other peaks can be the ternary $CoWO_4$ or binary WO_3.[36–38] Oxides such as Co_3O_4 and Cr_2O_3 correspond to oxidized elements from the Stellite 6 matrix and $CoWo_4$ and WO_3, most likely from tungsten carbide oxidation.[36–39] Fig. 9b presents the spectra obtained from the SWC coating. The overlap of the different peaks is more present; however, the main oxide seems to be the ternary $CoWO_4$ and binary

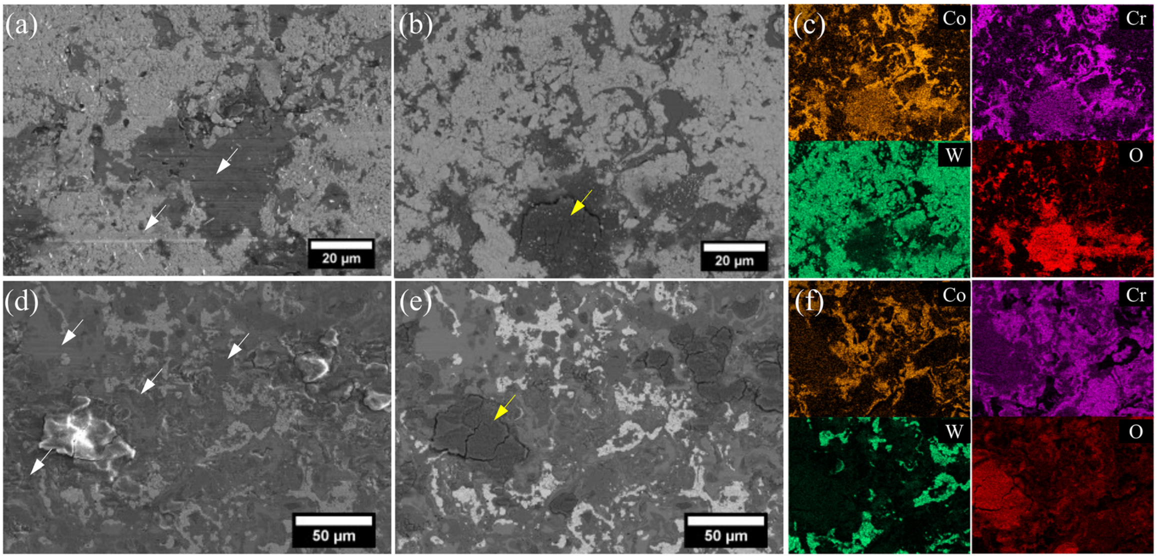

Fig. 7 Top view of the wear track of (a)–(c) Stellite6—WC-Ni coating and (d) and (e) Stellite6—Cr_3C_2—WC-Ni coating tested at RT for 5000 cycles. White arrows highlight the abrasive marks and yellow arrows the formation of tribolayers. EDS-mapping of (c) SW and (f) SWC coatings.

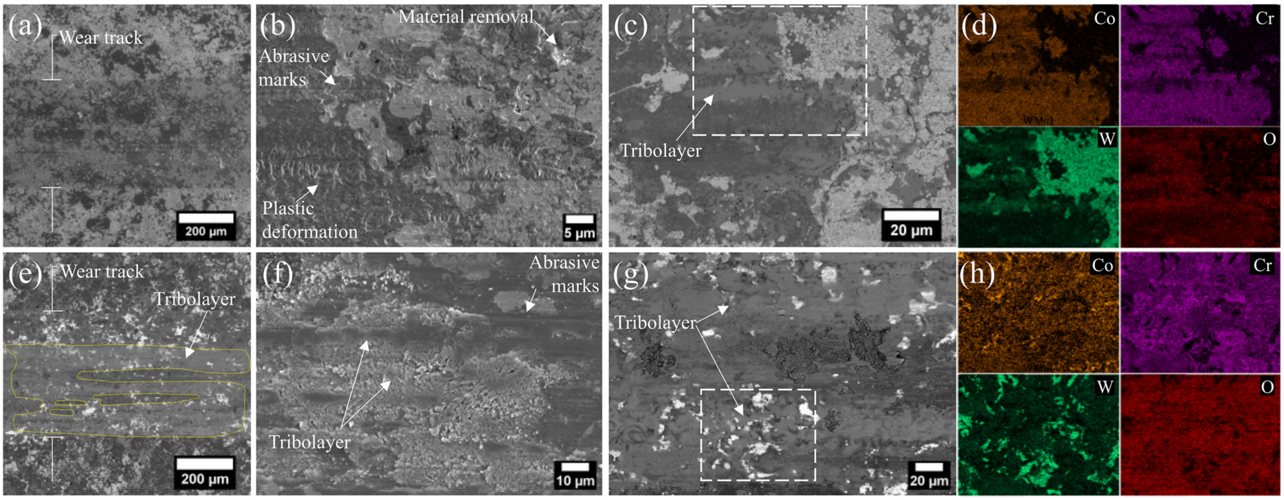

Fig. 8 Top view of the wear track of (a)–(c) Stellite6—WC-Ni coating and (e)–(g) Stellite6—Cr_3C_2—WC-Ni coating tested at 300 °C sliding for 20 000 cycles. EDS-mapping of (d) SW and (h) SWC coatings.

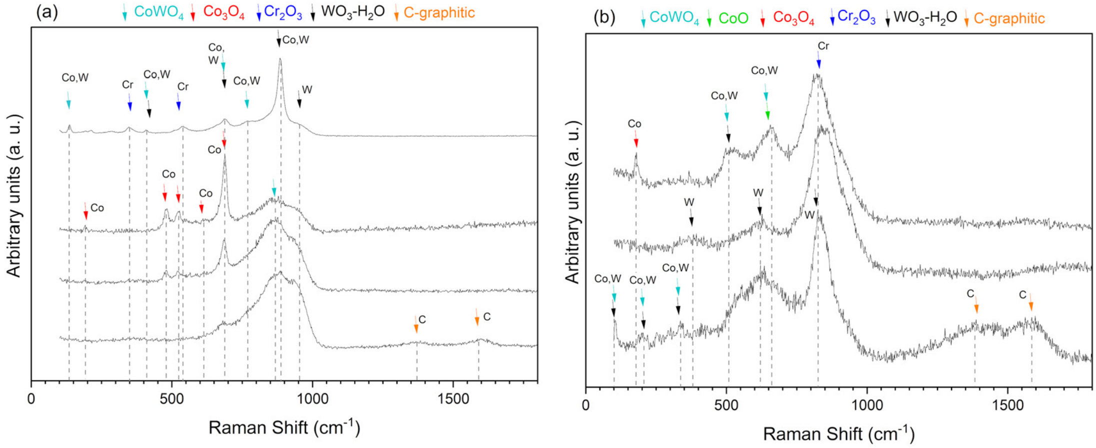

Fig. 9 Raman spectra of (a) SW (Stellite6—WC-Ni) and (b) SWC (Stellite6—WC-Ni—Cr_3C_2) coatings tested at 300 °C.

Cr_2O_3.[38,39] Other oxides are CoO, Co_3O_4, and WO_3.[36–38,40] The peaks close to the graphitic carbon suggest the presence of carbide particles mixed with the oxides.

Fig. 10 shows low and high-magnification micrographs of the cross-section of the SCW coating worn tracks. The cross-section revealed sub-cracks on the chromium carbides (Fig. 10a) and some regions with tribolayers (Fig. 10b). Elemental analysis on the tribolayers detected regions rich in Cr (36 Cr, 24 O, 16 W, 16 Co wt%, others) and similar analysis could be drawn from the EDS mapping shown in Fig. 11, showing a high concentration of Cr and O at the surface of the coating, in addition to Co and W.

The volume loss of the alumina counter balls for all conditions was measured in the order of 10^{-7} and 10^{-5} mm^3, and wear rate values in the range of 10^{-9} and 10^{-8} mm^3 N^{-1} m^{-1} for the SW and SCW coating, respectively. Fig. 12 presents the micrographs of the two coatings tested at room and elevated temperature for 5000 and 20 000 cycles. Transfer films are observed on the different wear balls. Fig. 12a highlights the transfer film of the alumina ball sliding against the SW coating containing bright particles related to a high W content (39 W, 24 O, 23 Al, 6 Co, 5 C, 3 Cr wt%) embedded in a matrix containing mainly Co (30 Al, 28 O, 20 Co, 11 W, 7 Cr, 4 C wt%). Sliding against the SW coating at an elevated temperature (300 °C) develops a transfer film covering the contact area, as seen in Fig. 12b and c. The elemental analysis revealed a similar composition high in W content after sliding for 5000 cycles (41 W, 23 O, 12 Al, 11 Co, 7 Ni, 5 Cr, 1 C wt%) or 20000 cycles (43 W, 19 O, 14 Co, 9 Al, 7 Ni, 6 Cr, 2 C wt%). Fig. 12d–f show the alumina balls sliding against the SCW coating. At room temperature, the small regions covered by a transfer film present a rich W content (39 O, 20 W, 20 Al, 13 Cr, 4 Co, 4 C wt%). And at elevated temperatures (300 °C), the transfer films that mostly covered the contact area showed a similar elemental distribution rich in Cr after sliding for 5000 cycles (29 Cr, 29 O, 18 W, 12 Co,

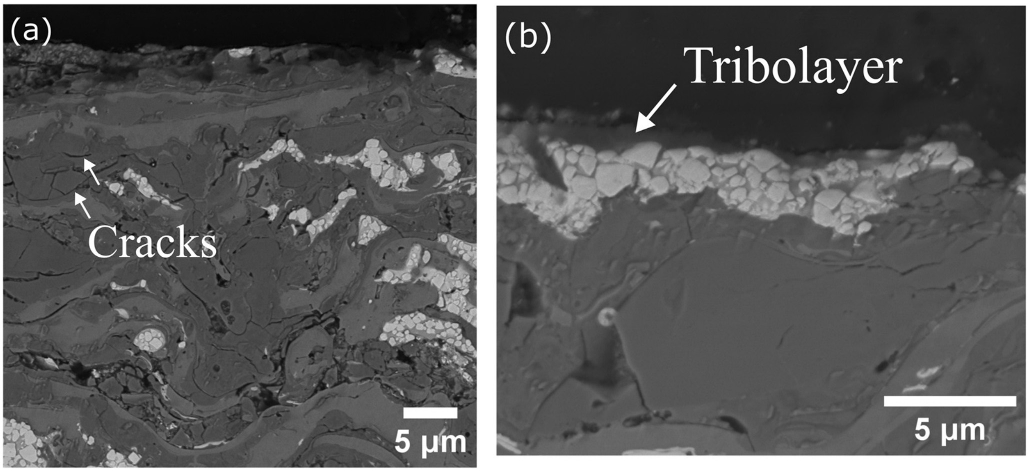

Fig. 10 Cross-section of the SWC worn coating after sliding 20 000 cycles at 300 °C. (a) Low and (b) high magnification highlighting the tribolayer. Sliding direction is left to right.

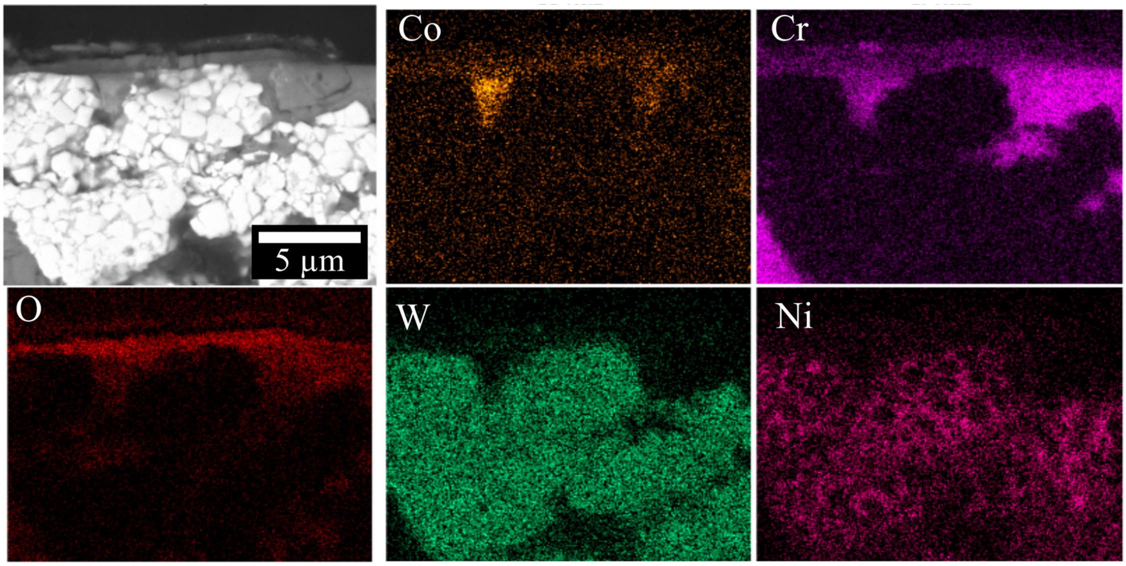

Fig. 11 EDS mapping of the SWC worn coating after sliding 20 000 cycles at 300 °C. Sliding direction from left to right.

10 Al, 2 C wt%) and 20 000 cycles (32 Cr, 26 O, 18 W, 12 Co, 7 Al, 3 Ni, 2 C).

Therefore, WC particles (identified by the Raman peaks, Fig. 9a) transferred to the alumina ball at room temperature promote the abrasive marks observed on the SW coating (Fig. 7a). The WC particles are mixed with Co-matrix, similar to the tribolayers formed on the SW coating (Fig. 7b), suggesting a Co-rich oxide film. On the contrary, no WC particles are observed on the alumina balls sliding against the SCW coating, which can be related to the less pronounced abrasive marks on this coating. At elevated temperatures, the transfer film can confirm the presence of the tungsten oxides observed on the worn surface of both coatings; however, the high Cr content can emphasize the main peak related to Cr_2O_3 on the Raman spectra for the SWC coating.

Conclusions

This study investigated the wear behavior at elevated temperatures of composite coatings based on Stellite 6 with additions of one or two types of carbides (WC-Ni and Cr_3C_2) produced *via* high-velocity oxygen fuel (HVOF) spraying. The composites presented an excellent wear resistance, in the order of 10^{-6} mm^{-3} N^{-1} m^{-1}.

The coatings presented a homogeneous distribution between the molten metallic splats and deformed carbide particles. The rapid solidification of HVOF spraying prevents the presence of dendritic or spike-like features in the metallic phase, segregation of intermetallics or carbides, and decarburization of the hard phase, unlike coatings containing WC and Cr_3C_2 found in the literature (typically produced as WC-Co, WC-CoCr, Cr_3C_2-Ni, and Cr_3C_2–WC-NiCoCr). The SWC coating

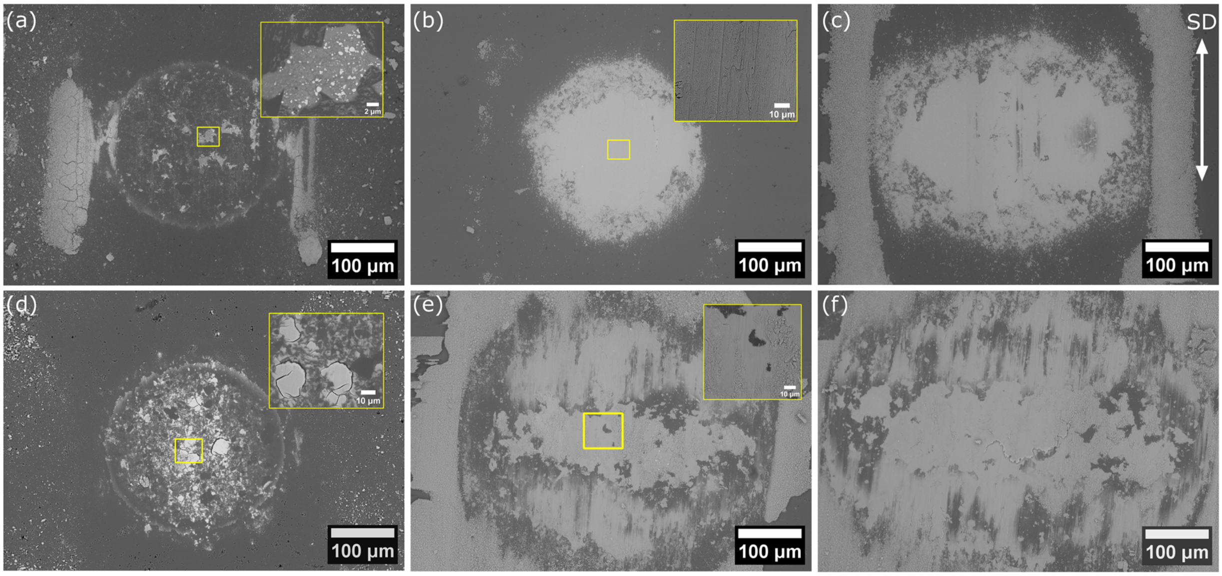

Fig. 12 Micrographs of the top view of the alumina counter ball sliding against SW coating at (a) RT, (b) 300 °C for 100 m, (c) 300 °C for 400 m and SWC coating at (d) RT, (e) 300 °C for 100 m, (f) 300 °C for 400 m.

exhibited higher hardness at both room temperature and elevated temperatures (300 °C) compared to the SW coating, which is attributed to its higher carbide content. Both coatings exhibited lower hardness at elevated temperatures due to the thermal softening of the metallic matrix and binder.

Wear tests at room temperature and 300 °C provided significant insights into the wear mechanisms. At room temperature, both coatings exhibited higher coefficients of friction (CoF) during the run-in period, followed by a steady state with minor differences in wear rate. The carbides provided load-bearing capacity, resulting in mainly abrasive marks on the metallic matrix, suggesting protection from significant damage. Minimal oxidative wear was observed with the formation of tribolayers rich in Co, Cr, and O at the centre of the wear track for both coatings.

At 300 °C, the SW coating showed an elevated CoF with a low wear rate, presenting primarily adhesive wear and a less predominant presence of abrasive and oxidative wear. The presence of W in the tribolayer at elevated temperatures differed from the results at room temperature. In contrast, the SWC coating showed a lower CoF and higher wear rate, particularly when comparing the results after 5000 cycles. After 20 000 cycles, the oxidative wear of the SWC coating with a tribolayer formation led to a significant drop in CoF and wear rate (compared to 5000 cycles). The tribolayer consists of different oxides, and a significant presence of Cr was detected by EDS and Raman spectroscopy.

Although the alumina ball slid against hard coatings, its wear rate remained low, ranging from 10^{-9} to 10^{-8} mm^3 N^{-1} m^{-1} for the SW and SWC coatings, respectively, due to the formation of a transfer film on the coatings.

The results highlight the distinct roles of carbides in determining the mechanical and tribological properties of the coatings. The SW coating, with WC-Ni, outperformed the SWC coating in terms of wear resistance at elevated temperatures. Tungsten carbide, although effective in load-bearing, did not contribute as significantly to tribolayer formation, causing the CoF to remain constant up to 20 000 cycles. In contrast, the addition of chromium carbide promotes the formation of a protective tribolayer, reducing the CoF.

The advantage of spraying a cobalt-based alloy (Stellite 6) in combination with WC-Ni or Cr_3C_2 coating using HVOF is the ability to tailor the distribution, chemistry, phase distribution, and microstructure of the metallic and carbide phases. Overall, the results underscore the potential of these composite coatings for applications requiring high wear resistance at elevated temperatures.

Author contributions

Conceptualization, A. I. E., M. M., P. S., C. M. and R. R. C.; methodology, A. I. E., P. S., C. M. and R. R. C.; investigation, A. I. E.; resources, M. M., C. M. and R. R. C.; writing – original draft preparation, A. I. E.; writing – review and editing, R. R. C.; visualization, A. I. E.; supervision, C. M. and R. R. C.; project administration, M. M., C. M. and R. R. C.; funding acquisition, M. M., P. S., C. M. and R. R. C. All authors have read and agreed to the published version of the manuscript.

Conflicts of interest

There are no conflicts to declare.

Data availability

The data supporting this article have been included in the main text and as part of the supplementary information (SI).

Supplementary information is available. See DOI: https://doi.org/10.1039/d5ma01042j.

Any further details will be available upon request.

Acknowledgements

This research was funded by the Natural Sciences and Engineering Research Council (NSERC) (project number CRDPJ 530409-18) and the Consortium for Research and Innovation in Aerospace in Quebec (CRIAQ) (project number MANU-1719), and a McGill Engineering Doctoral Award (MEDA) and CONAHCyT (CVU-638758) awarded to A. I. E. The authors would like to acknowledge the support of Fadhel Ben Ettouil with the coating deposition; and Eutectic Canada for supplying the powders used in this project

References

1 I. M. Hutchings and P. Shipway, *Tribology: friction and wear of engineering materials*, Butterworth-Heinemann, an imprint of Elsevier, Oxford, 2nd edn, 2017.
2 E. Ross, A. Ignatov and P. Stoyanov, *Tribol. Ind.*, 2021, **43**, 465–469.
3 R. R. Chromik and Y. Zhang, *Curr. Opin. Solid State Mater. Sci.*, 2018, **22**, 142–155.
4 B. C. N. M. de Castilho, N. Sharifi, S. A. Alidokht, K. Harrington, P. Stoyanov, C. Moreau and R. R. Chromik, *Wear*, 2021, **477**, 203892.
5 A. Dreano, S. Fouvry and G. Guillonneau, *Wear*, 2020, 452–453.
6 P. J. Blau, *Tribol. Int.*, 2010, **43**, 1203–1208.
7 N. Chelliah and S. V. Kailas, *Wear*, 2009, **266**, 704–712.
8 J. R. Davis and A. S. M. I. H. Committee, *Nickel, cobalt, and their alloys*, ASM International, Materials Park, OH, 2000.
9 M. X. Yao, J. B. C. Wu, W. Xu and R. Liu, *Mater. Sci. Eng. A*, 2005, **407**, 291–298.
10 G. Kong, D. Zhang, P. D. Brown, D. G. McCartney and S. J. Harris, *Mater. Sci. Technol.*, 2003, **19**, 1003–1011.
11 G. Bolelli and L. Lusvarghi, *J. Therm. Spray Technol.*, 2006, **15**, 802–810.
12 R. Ahmed, O. Ali, C. C. Berndt and A. Fardan, *J. Therm. Spray Technol.*, 2021, **30**, 800–861.
13 T. S. Cherepova and G. P. Dmitrieva, *Powder Metall. Met. Ceram.*, 2016, **55**, 374–378.
14 S. A. Alidokht, P. Manimunda, P. Vo, S. Yue and R. R. Chromik, *Surf. Coat. Technol.*, 2016, **308**, 424–434.
15 J.-N. Aoh and J.-C. Chen, *Wear*, 2001, **250**, 611–620.
16 V. Matikainen, G. Bolelli, H. Koivuluoto, P. Sassatelli, L. Lusvarghi and P. Vuoristo, *Wear*, 2017, **388–389**, 57–71.
17 L.-M. Berger, S. Saaro, T. Naumann, M. Kašparova and F. Zahálka, *J. Therm. Spray Technol.*, 2008, **17**, 395–403.
18 Z. Xie, C. Zhang, R. Wang, D. Li, Y. Zhang, G. Li and X. Lu, *J. Mater. Res. Technol.*, 2021, **15**, 821–833.
19 L.-M. Berger, M. Woydt and S. Saaro, *Wear*, 2009, **266**, 406–416.
20 L.-M. Berger, *Int. J. Refract. Met. Hard Mater.*, 2015, **49**, 350–364.
21 L. M. Berger, *IOP Conf. Ser.*, 2016, **118**, 012010.
22 S. A. Alidokht, J. Lengaigne, J. E. Klemberg-Sapieha, S. Yue and R. R. Chromik, *J. Mater. Eng. Perform.*, 2019, **28**, 1532–1543.
23 R. J. Alroy, M. Kamaraj and G. Sivakumar, *Surf. Coat. Technol.*, 2023, **463**, 129498.
24 S. K. Asl, M. H. Sohi, K. Hokamoto and M. Uemura, *Wear*, 2006, **260**, 1203–1208.
25 G. Bolelli, L.-M. Berger, M. Bonetti and L. Lusvarghi, *Wear*, 2014, **309**, 96–111.
26 J. M. Guilemany, J. M. Miguel, S. Vizcaino and F. Climent, *Surf. Coat. Technol.*, 2001, **140**, 141–146.
27 V. Katranidis, S. Gu, T. R. Reina, E. Alpay, B. Allcock and S. Kamnis, *Surf. Coat. Technol.*, 2017, **328**, 499–512.
28 V. Matikainen, G. Bolelli, H. Koivuluoto, M. Honkanen, M. Vippola, L. Lusvarghi and P. Vuoristo, *J. Therm. Spray Technol.*, 2017, **26**, 1239–1256.
29 B. Song, M. Bai, K. T. Voisey and T. Hussain, *J. Therm. Spray Technol.*, 2017, **26**, 554–568.
30 J. R. Davis, *Associates and A. S. M. I. T. S. S. T. Committee, Handbook of thermal spray technology*, ASM International, Materials Park, OH, 2004.
31 G. M. Smith, E. J. Gildersleeve, X.-T. Luo, V. Luzin and S. Sampath, *Surf. Coat. Technol.*, 2020, **387**, 125536.
32 V. N. V. Munagala, T. B. Torgerson, T. W. Scharf and R. R. Chromik, *Wear*, 2019, **426–427**, 357–369.
33 M. Godet, *Wear*, 1984, **100**, 437–452.
34 J.-N. Aoh, Y.-R. Jeng, E.-L. Chu and L.-T. Wu, *Wear: Part 2*, 1999, **225**, 1114–1122.
35 A. Islas Encalada, S. A. Alidokht, N. Sharifi, P. Stoyanov, M. Makowiec, C. Moreau and R. R. Chromik, *Wear*, 2024, **546–547**, 205310.
36 V. G. Hadjiev, M. N. Iliev and I. V. Vergilov, *J. Phys. C-Solid State Phys.*, 1988, **21**, L199.
37 M. F. Daniel, B. Desbat, J. C. Lassegues, B. Gerand and M. Figlarz, *J. Solid State Chem.*, 1987, **67**, 235–247.
38 M. Boulova, N. Rosman, P. Bouvier and G. Lucazeau, *J. Phys.: Condens. Matter*, 2002, **14**, 5849–5863.
39 D. A. Brown, D. Cunningham and W. K. Glass, *Spectrochim. Acta, Part A*, 1968, **24**, 965–968.
40 D. J. Gardiner, P. R. Graves and H. J. Bowley, *Practical Raman Spectroscopy*, Springer-Verlag, Berlin, 1989.